Composites Communications 24 (2021) 100675

Contents lists available at ScienceDirect

Composites Communications

journal homepage: www.elsevier.com/locate/coco

Controllable synthesis of sulfurized polyacrylonitrile nanofibers for high performance lithium–sulfur batteries

Huilan Li [a], Wenying Xue [a], Wangcong Xu [a], Lina Wang [a,*], Tianxi Liu [a,b]

[a] State Key Laboratory for Modification of Chemical Fibers and Polymer Materials, College of Materials Science and Engineering, Innovation Center for Textile Science and Technology, Donghua University, Shanghai, 201620, China
[b] Key Laboratory of Synthetic and Biological Colloids, Ministry of Education, School of Chemical and Material Engineering, Jiangnan University, Wuxi, 214122, China

ARTICLE INFO

Keywords:
Sulfurized polyacrylonitrile
Nanofibers
Synthesis temperature
Lithium–sulfur batteries

ABSTRACT

Sulfurized polyacrylonitrile (SPAN) is regarded to be one of the most promising cathode materials for lithium–sulfur (Li–S) batteries because of its unique chemical structure and high cyclic ability. However, the physicochemical properties of SPAN correlate with the synthesis and process conditions. In this work, flexible and freestanding SPAN nanofiber cathodes are prepared via the electrospinning technique followed by a sulfurization process. And the effect of synthesis temperatures on microstructure and electrochemical performance of SPAN are systematically investigated. According to the spectroscopic analysis, short $-S_x-$ ($2 \leq x \leq 3$) chains are covalently bonded to the cyclized and dehydrogenated PAN backbones through C–S bonds during the synthesis temperature between 300 and 600 °C. Among which, the SPAN nanofiber prepared at 500 °C shows not only a low charge transfer resistance but also the best cell performance. Upon 200 cycles, it displays a high reversible capacity of 1280 mAh g^{-1} with a fading rate as low as 0.02% per cycle at 400 mA g^{-1}. Highly stable long-term cycling at higher current densities and good rate capability are also achieved. The work provides significant guidance for the development of advanced SPAN cathode materials.

1. Introduction

As the requirements of portable devices and large-scale power source increases, the development of new rechargeable systems with high energy density, low cost and long life-span is of great significance [1–5]. Owing to the natural abundance and high theoretical capacity (1675 mAh g^{-1}) of elemental sulfur (S_8) [3,6–8], lithium–sulfur (Li–S) battery has attracted significant attentions. However, the application of Li–S batteries has been blocked by the inherent drawbacks of S_8 cathode. The main issues are originated from the poor conductivity of S_8 and the final discharge product of Li_2S, the shuttling of soluble lithium polysulfide intermediates (Li_2S_n, $2 < n \leq 8$) and the massive volume changes of sulfur cathode during the lithiation/delithiation processes [2,8–12].

Numerous attempts have been executed to tackle the challenges by confining sulfur in porous carbon hosts [8,13–15] or employing functional polar sites to anchor polysulfides [7,16–18], etc. In addition, to chemically trap sulfur in pyrolyzed polymer backbones via chemical bonds is another plausible approach. Among which, sulfurized polyacrylonitrile (SPAN) has been regarded as the most promising candidate for its better cyclic stability and lower self-discharge than S_8 cathode [19–22]. SPAN materials show high compatibility with carbonate electrolytes, in which the formation of soluble polysulfides is successfully avoided, leading to the high utilization of sulfur. In spite of the advantages, the saturated sulfur content in SPAN is generally less than 45 wt% [21,22], which prevents the realization of high energy density Li–S batteries. To address this issue, a freestanding SPAN electrode without large amounts of inactive carbon additives and polymer binders is a rational choice [21]. Nonetheless, the physicochemical properties of SPAN rely heavily on the synthesis conditions. Fanous et al. synthesized the pulverous SPAN material at 330 °C and obtained a capacity of 1250 mAh g^{-1} at the current rate of 0.1 C (1 C = 1675 mA g^{-1}) after 40 cycles [23]. When the synthesis temperature increased to 550 °C, the SPAN delivered a capacity of 1429 mAh g^{-1} at 0.1 C after 40 cycles [24]. The SPAN synthesized at 400 °C by Wang et al. showed a capacity of 1332 mAh g^{-1} at 0.1 C after 50 cycles [25]. It can be seen that the sulfurization temperature is a vital factor affecting the electrochemical performance of SPAN. Therefore, it is crucial to clarify the suitable synthesis conditions for the preparation of freestanding SPAN cathodes.

Herein, we investigate the effect of synthesis conditions on the performance of freestanding fibrous SPAN cathodes, which are prepared

* Corresponding author.
E-mail address: linawang@dhu.edu.cn (L. Wang).

https://doi.org/10.1016/j.coco.2021.100675
Received 27 January 2021; Received in revised form 5 February 2021; Accepted 6 February 2021
Available online 17 February 2021

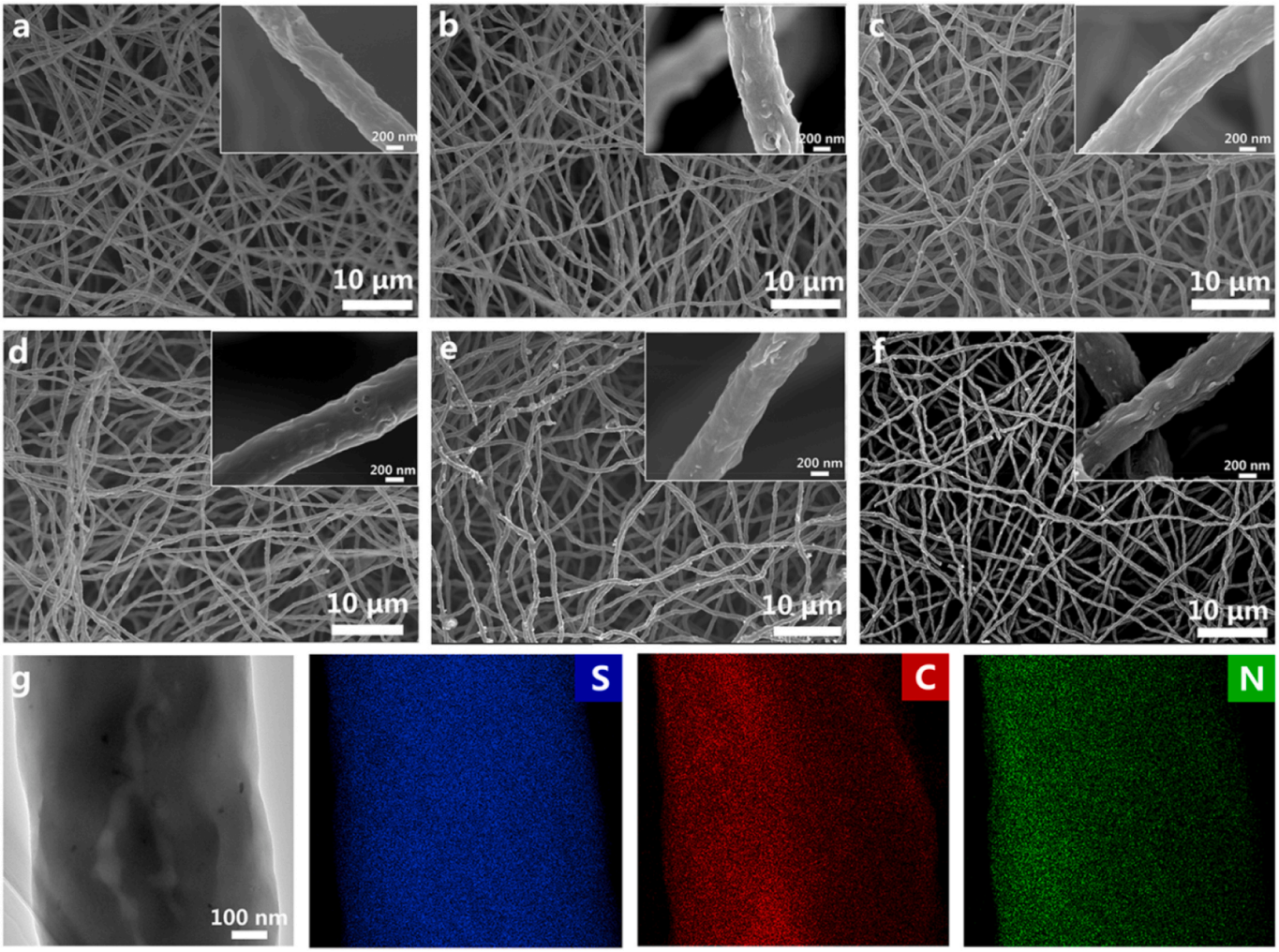

Fig. 1. Top-view SEM images of (a) PAN/CNT, (b) SPAN/CNT-300, (c) SPAN/CNT-400, (d) SPAN/CNT-500, (e) SPAN/CNT-600 and (f) SPAN/CNT-700 films. The inset boxes are images with high magnifications. (g) TEM image of single SPAN/CNT-500 nanofiber and the corresponding elemental mappings of S, C and N.

through the electrospinning technique followed by a sulfurization process at various temperatures. The spectroscopic characterizations reveal that the C–S/S–S bonds can be readily formed in SPAN upon sulfurization between 300 and 600 °C. The fundamental but systematic electrochemical tests of SPAN nanofibers suggest the optimized synthesis temperature is 500 °C. The SPAN cathode prepared at 500 °C delivers the highest reversible capacity of 1280 mAh g^{-1} with a slow fading rate of 0.02% per cycle after 200 cycles at 400 mA g^{-1}.

2. Experimental section

2.1. Synthesis of freestanding SPAN/CNT nanofibers

In a typical preparation procedure, 1.0 g polyacrylonitrile (PAN, M_w = 150000, Sigma-Aldrich) and 0.12 g multiwalled carbon nanotubes (CNTs, 98% purity) with a diameter of ca. 10–20 nm were added into 9.0 g N,N-dimethylformamide (DMF, 99.5%, Shanghai Lingfeng Chemical) and magnetically stirred overnight. The obtained homogeneous precursor solution was transferred into an injection syringe with a metallic needle and the applied working voltage was 18 kV. The feed rate of the precursor solution was 1.6 mL h^{-1}, and the interval from the needle to the Al foil collector was set to 24 cm. The as-spun film was denoted as PAN/CNF. SPAN/CNT films were prepared by heating PAN/CNT with sublimed sulfur (chemical purity, Sinopharm Chemical) at different temperatures for 3 h in a tube furnace under a nitrogen atmosphere. In order to ensure the complete sulfurization of PAN/CNT, the weight ratio of PAN to sulfur is 1:10. The samples synthesized at 300, 400, 500, 600 and 700 °C are marked as SPAN/CNT-300, SPAN/CNT-400, SPAN/CNT-500, SPAN/CNT-600 and SPAN/CNT-700, respectively. In addition, a controlled sulfur-free freestanding pyrolyzed PAN/CNT denoted as pPAN/CNT was prepared as well.

2.2. Material characterizations

The morphological structures of the as-prepared materials were observed by scanning electron microscopy (SEM, JSM-7500F, JEOL) and transmission electron microscopy (TEM, JEM-2100F, JEOL) coupled with an energy dispersive X-ray spectrometer (EDS). The X-ray diffraction (XRD) patterns were recorded with an X-ray diffractometer by using Cu Kα radiation (D/max-2550VB+/PC, Rigalcu). The Raman spectra were collected on inVia Reflex Raman Spectrometer (inVia-Reflex, Renishaw). Fourier transform infrared (FTIR) spectra were acquired on the Bruker VECTOR22 FTIR spectrometer. X-ray photoelectron spectroscopy (XPS) spectra were collected by Escalab 250Xi spectrometer with a monochromatic Al Kα X-ray source. Elemental analysis (Vario EL III, Elementar, Germany) was used to measure the sulfur contents. The thermal gravimetric analysis (TGA) of as-prepared samples was investigated by the thermogravimetric analyzer (NETZSCH TG 209 F1 Libra) in nitrogen atmosphere.

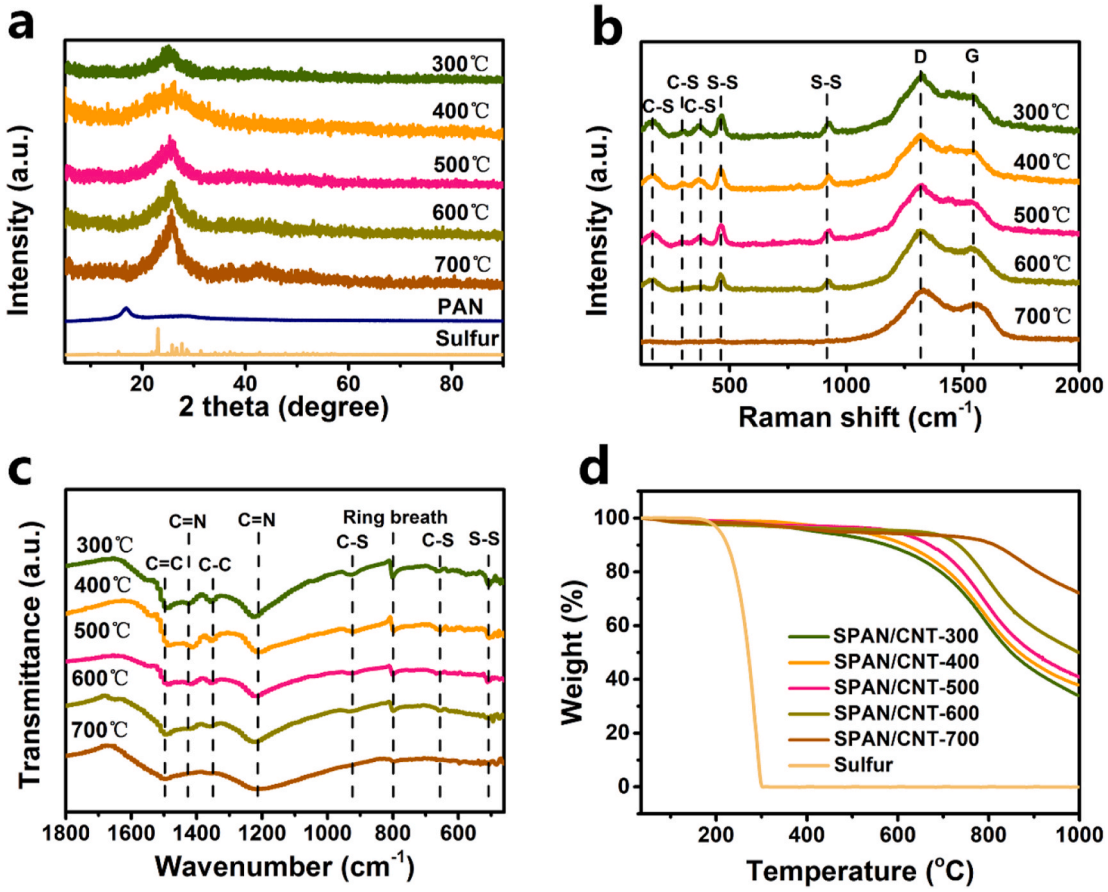

Fig. 2. (a) XRD patterns of PAN, elemental sulfur and SPAN/CNT composites. (b) Raman spectra, (c) FTIR spectra and (d) TGA curves of SPAN/CNT prepared at 300–700 °C.

2.3. Electrochemical measurements

Round disks with a diameter of 12 mm were sliced from the SPAN/CNT films and used directly as the cathodes. The electrochemical characteristics of SPAN/CNT were measured using the coin cells (CR2025) with polypropylene/polyethylene (PP/PE) membrane (Celgard 2325) as separator and Li metal as anode. The electrolyte is composed of 1 M lithium bis(trifluoromethanesulfone)imide (LiTFSI) in 1,3-dioxolane (DOL)/1,2-dimethoxyethane (DME) (v/v = 1:1) with 0.2 M $LiNO_3$ (Shanghai Songjingenergy Co., Ltd). Land battery station (CT2001A) was utilized to test the galvanostatic charge/discharge performance within the voltage region of 1–3 V (vs Li/Li^+). Cyclic voltammetry (CV) was tested by the electrochemical workstation (Arbin Instruments, USA) with a scan rate of 0.05 mV s^{-1} between 1.0 and 3.0 V. Electrochemical impedance spectroscopy (EIS) was tested on a CHI660E electrochemical workstation in the frequency range of 0.1 Hz–100 kHz.

3. Results and discussion

The fibrous SPAN/CNT films were synthesized through electrospinning and sulfurization process. Firstly, the PAN/CNT precursor films were made from the homogeneous solution containing PAN, DMF and CNTs via electrospinning technique. Subsequently, elemental sulfur was heated together with PAN/CNT films under nitrogen atmosphere at different temperatures for 3 h, respectively. The morphological structure of PAN/CNT precursor film and SPAN/CNT films were observed by SEM. The nanofibers of both PAN/CNT (Fig. 1a) and SPAN/CNT (Fig. 1b–f) show a rough surface due to the presence of CNTs. The interconnected network structure is maintained before and after sulfurization irrespective of synthesis temperatures. The diameter of PAN/CNT nanofibers is ca. 400 nm (inset Fig. 1a), which increases to ca. 500 nm after sulfurization at 300–600 °C (inset Fig. 1b–e), owing to the infiltrated saturated sulfur species. Whereas, the diameter of the SPAN/CNT-700 nanofibers does not inflate, which is ca. 400 nm (inset Fig. 1f), indicating an insufficent infiltration of sulfur at 700 °C. Homogeneous elemental distributions of S, C and N are achieved for all of the samples. To illustrate, the EDS elemental mapping images of SPAN/CNT-500 (Fig. 1g) and SPAN/CNT-700 (Fig. S1) as examples, revealing that the distributions of S, C and N elements are uniform in SPAN/CNT nanofibers. Compared with that of SPAN/CNT-500, the density of S in SPAN/CNT-700 is however obviously sparsely, indicating a lower sulfur content.

XRD was employed to identify the crystal structure of SPAN/CNT materials (Fig. 2a), along with that of elemental sulfur and PAN. Compared with elemental sulfur that displays many characteristic sharp diffraction peaks, the absence of these peaks in SPAN/CNT indicates the amorphous phase of sulfur. The characteristic peak of PAN at 17° is also not observed, instead a peak located at 26.5° attributing to the graphitic (002) plane becomes sharper with increasing of synthesis temperatures, indicating an increased degree of carbonization [25]. A higher degree of graphitization would lead to an increased electronic conductivity [26]. The chemical structure of the SPAN/CNT composites was investigated by Raman and FTIR spectroscopy. In the Raman spectra of SPAN/CNT synthesized at 300–600 °C (Fig. 2b), the peaks located at 176, 296 and 373 cm^{-1} are attributed to C–S bonds and that at 460 and 930 cm^{-1} are assigned to S–S bonds, implying that sulfur atoms are covalently bonded onto pyrolyzed PAN backbones [21,27–29]. The signals of covalently bonded sulfur are detected by FTIR as well (Fig. 2c). The characteristic peaks at 941 and 671 cm^{-1} can be ascribed to the ring breathing and stretch of C–S bonds. And the peak at 513 cm^{-1} corresponds to S–S

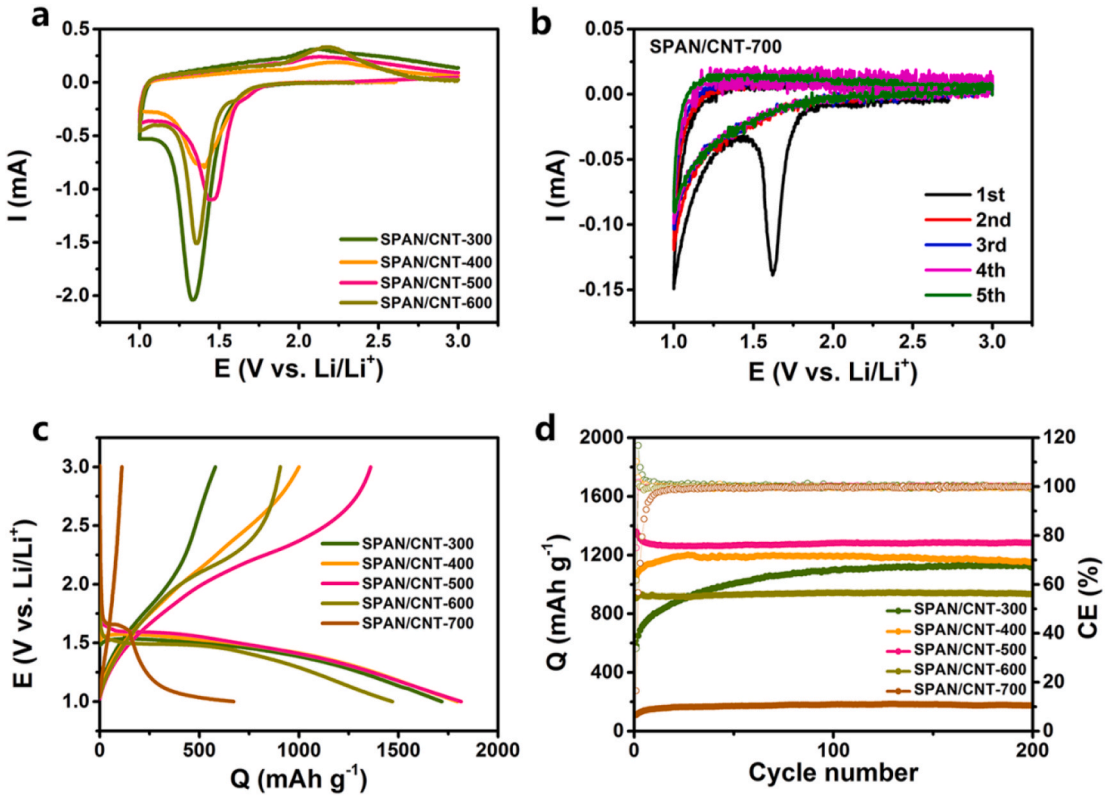

Fig. 3. Electrochemical feature of SPAN/CNT composites prepared at different temperatures. CV profiles of SPAN/CNT prepared at (a) 300–600 °C and (b) 700 °C. The sweep rate is 0.05 mV S^{-1}. (c) The galvanostatic charge−discharge profiles at the first cycle at 400 mA g^{-1}. (d) The corresponding cyclic performance at 400 mA g^{-1}.

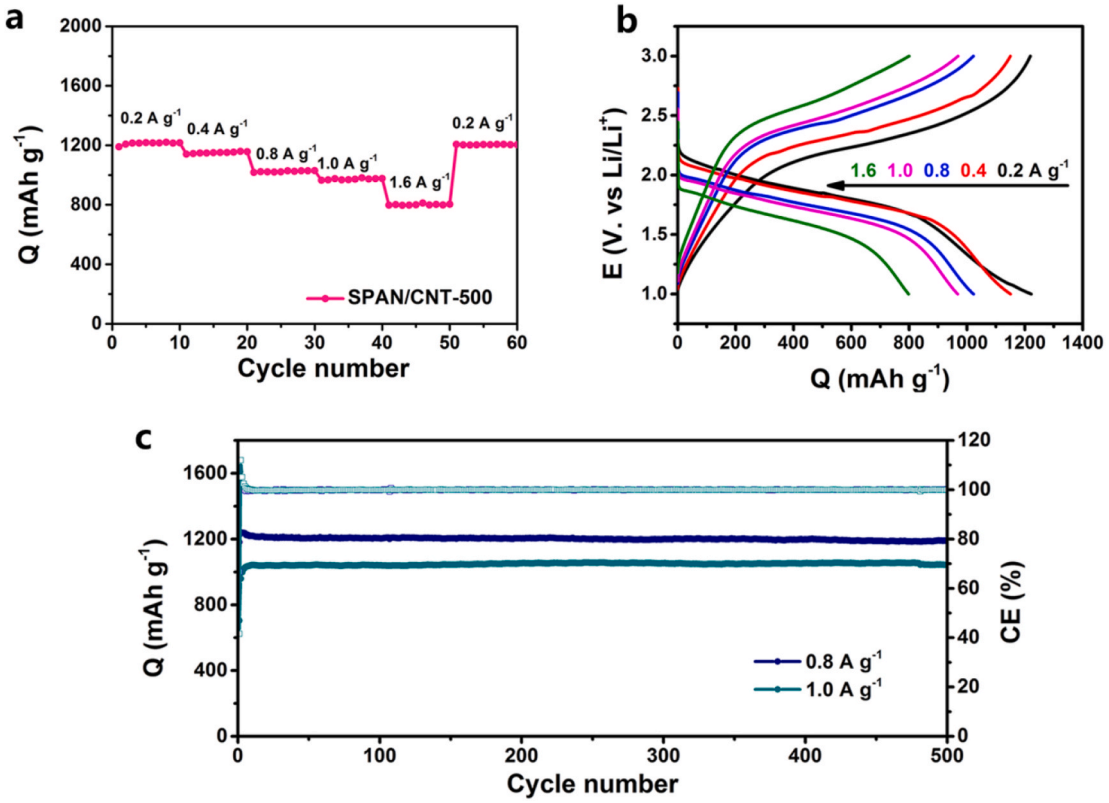

Fig. 4. (a) Rate capability of SPAN/CNT-500. (b) The corresponding galvanostatic charge–discharge profiles at different current densities. (c) Cyclic performance at 800 and 1000 mA g^{-1}.

stretch [21]. However, the characteristic peaks of C–S/S–S bonds in Raman and FTIR are very weak for SPAN/CNT-700, indicating fewer H atoms left on the pyrolyzed backbones to react with sulfur species due to the severe pyrolyzation of PAN at 700 °C. The SPAN/CNT may become a ladder-structure at the high heating temperature owing to the intermolecular cross-link and denitrogenation [22,30]. The results are in agreement with elemental analysis in Table S1. The sulfur content in SPAN/CNT decreases from 41.05 to 17.78 wt% with increasing of synthesis temperature from 300 to 700 °C. Fig. 2d shows the TGA of elemental sulfur and SPAN/CNT prepared at 300–700 °C. Elemental sulfur exhibits a thorough weight loss of 100% at 180–300 °C. Instead, SPAN/CNT composites start to lose weight beyond 400 °C. With increasing of synthesis temperature, the weight-loss temperature increases gradually, indicating the stronger covalent bond between S atoms and pyrolyzed backbones. The chemical states of the elements were explored by XPS (Fig. S2). Take the survey spectrum of SPAN/CNT-500 for instance, signals of C 1s, S 2p and N 1s can be detected (Fig. S2a). The C 1s (Fig. S2b) and S 2p (Fig. S2c) spectra also confirm the formation of C–S/S–S bonds. The N 1s spectrum consists of two peaks at 398.5 and 400.0 eV, corresponding to pyridinic and pyrrolic nitrogen atoms [21,31–33], further confirming the cross-linking of PAN during the sulfurization process (Fig. S2d).

Electrochemical performance tests were carried out to evaluate the influence of synthesis temperature on SPAN/CNT. The CV test was performed within the voltage region of 1.0–3.0 V. In the initial cathodic scan, the reduction peak at 1.3–1.5 V of SPAN/CNT synthesized from 300 to 600 °C is attributed to lithiation of SPAN (Fig. 3a), leading to the formation of the end-product Li_2S. Upon the reverse anodic scan, the oxidation peak in the voltage of 2.1–2.2 V corresponds to the conversion from Li_2S to C–S/S–S bonds in SPAN. Among the CV curves, the SPAN/CNT-500 exhibits the lowest voltage polarization between the cathodic and anodic peaks, suggesting a fast reaction kinetics. The EIS spectra of the fresh cells shield more light on the better reaction kinetics of SPAN/CNT-500 (Fig. S3). The cell with SPAN/CNT-500 shows a lower charge transfer resistance (20.70 Ω) than that with SPAN/CNT-300 (32.96 Ω). However, the SPAN/CNT-700 shows a poor reversibility, implying that the chemical structure of SPAN/CNT-700 is not well recovered (Fig. 3b). The extraordinary strong covalent bonding of S atoms to pyrolyzed backbones may affect the smooth reversible reaction of SPAN/CNT-700. The galvanostatic charge–discharge profiles of SPAN/CNT are consistent with the CV curves (Fig. 3c). At the current density of 400 mA g^{-1}, the initial discharge specific capacities of SPAN/CNT prepared from 300 to 700 °C are 1717, 1796, 1814, 1469 and 672 mAh g^{-1}, and charge specific capacities are 580, 1000, 1359, 906 and 111 mAh g^{-1}, respectively. The SPAN/CNT-500 delivers the highest initial coulombic efficiency of 74.9%. Moreover, a superior cyclic performance is obtained as well for SPAN/CNT-500, retaining a superior specific capacity of 1280 mAh g^{-1} with a small degradation of 0.02% per cycle after 200 cycles (Fig. 3d). It should be noted that the capacity contribution of pyrolyzed backbone can be ignored in the voltage of 1–3 V. As confirmed by the cell performance of the freestanding pPAN/CNT, which can only deliver a specific capacity less than 10 mAh g^{-1} after the first cycle at 200 mA g^{-1} (Fig. S4). The result suggests 500 °C is the optimum temperature for the synthesis of the SPAN/CNT nanofibers. The SPAN/CNT prepared at lower temperatures suffer from a higher charge transfer resistance and that prepared at higher temperatures cannot achieve smooth lithiation/delithiation processes due to a higher C–S bonding energy, leading to unsatisfied electrochemical performance.

The rate capability provides further convincing evidence of the superiority of SPAN/CNT-500 (Fig. 4a). The average specific capacities are 1215, 1150, 1020, 970 and 810 mAh g^{-1} at 200, 400, 800, 1000 and 1600 mA g^{-1}, respectively. The corresponding voltage profiles of SPAN/CNT-500 show the typical one pair of sloped voltage plateaus at ca. 2 V (Fig. 4b). The long-term cyclic performance at moderate current densities of 800 and 1000 mA g^{-1} demonstrates the stability of SPAN/CNT-500 (Fig. 4c). Even after 500 cycles, the battery maintains reversible capacities of 1192 at 800 mA g^{-1} and 1044 mAh g^{-1} at 1000 mA g^{-1}, respectively. The good tolerance of the cell to high current conditions and the high cyclic stability verify the advantages of the freestanding SPAN/CNT nanofibers.

4. Conclusions

In summary, a series of flexible and freestanding fibrous SPAN/CNT cathodes were prepared through the electrospinning followed by a sulfurization process at different temperatures. According to elemental mapping and XRD patterns, the sulfur in an amorphous state uniformly distributes in the SPAN/CNT nanofibers. In terms of elemental analysis, the sulfur content in SPAN/CNT decreases with increasing synthesis temperature. The spectroscopic characterizations confirm that C–S and S–S bonds are clearly detectable in SPAN/CNT within synthesis temperature between 300 and 600 °C. The superior electrochemical performance of SPAN/CNT-500 suggests 500 °C is the optimum sulfurization temperature. Impressively, the SPAN/CNT-500 delivers a high reversible capacity of 1280 mAh g^{-1} with a small capacity degradation of 0.02% per cycle after 200 cycles at 400 mA g^{-1}. The long-term cyclic stability and high rate capability provide further positive prospect for the practical applications of SPAN cathode materials.

CRediT authorship contribution statement

Huilan Li: Investigation, Methodology, Writing - original draft, Writing - review & editing, Software, Visualization. **Wenying Xue:** Data curation, Visualization. **Wangcong Xu:** Data curation, Visualization. **Lina Wang:** Methodology, Writing - original draft, Writing - review & editing, Visualization, Supervision, Funding acquisition. **Tianxi Liu:** Supervision, Funding acquisition.

Declaration of competing interest

The authors declare that they have no known competing financial interests or personal relationships that could have appeared to influence the work reported in this paper.

Acknowledgements

This work was supported by the National Natural Science Foundation of China (21603030), the Natural Science Foundation of Shanghai (17ZR1446400), and the Shanghai Scientific and Technological Innovation Project (18JC1410600).

Appendix A. Supplementary data

Supplementary data to this article can be found online at https://doi.org/10.1016/j.coco.2021.100675.

References

[1] X. Ji, K.T. Lee, L.F. Nazar, A highly ordered nanostructured carbon–sulphur cathode for lithium–sulphur batteries, Nat. Mater. 8 (2009) 500–506.
[2] A. Manthiram, Y. Fu, S.-H. Chung, C. Zhu, Y.-S. Su, Rechargeable lithium–sulfur batteries, Chem. Rev. 114 (2014) 11751–11787.
[3] L. Wang, Y. Zhao, M.L. Thomas, H.R. Byon, In situ synthesis of bipyramidal sulfur with 3D carbon nanotube framework for lithium–sulfur batteries, Adv. Funct. Mater. 24 (2014) 2248–2252.
[4] C. Qi, L. Xu, J. Wang, H. Li, C. Zhao, L. Wang, T. Liu, Titanium-containing metal–organic framework modified separator for advanced lithium–sulfur batteries, ACS Sustain. Chem. Eng. 8 (2020) 12968–12975.
[5] Y. Tian, Y. An, C. Wei, H. Jiang, S. Xiong, J. Feng, Y. Qian, Recently advances and perspectives of anode-free rechargeable batteries, Nano Energy 78 (2020) 105344.
[6] S.-H. Chung, A. Manthiram, Current status and future prospects of metal–sulfur batteries, Adv. Mater. 27 (2019) 1901125.
[7] H. Li, X. Wang, C. Qi, C. Zhao, C. Fu, L. Wang, T. Liu, Self-assembly of MoO_3-decorated carbon nanofiber interlayers for high-performance lithium–sulfur batteries, Phys. Chem. Chem. Phys. 22 (2020) 2157–2163.

[8] J. Zhang, C.-P. Yang, Y.-X. Yin, L.-J. Wan, Y.-G. Guo, Sulfur encapsulated in graphitic carbon nanocages for high-rate and long-cycle lithium–sulfur batteries, Adv. Mater. 28 (2016) 9539–9544.
[9] Y. Fan, Z. Niu, F. Zhang, R. Zhang, Y. Zhao, G. Lu, Suppressing the shuttle effect in lithium–sulfur batteries by a UiO-66-modified polypropylene separator, ACS Omega 4 (2016) 10328–10335.
[10] W. Zong, C. Yang, L. Mo, Y. Ouyang, H. Guo, L. Ge, Y. Miao, D. Rao, J. Zhang, F. Lai, T. Liu, Elucidating dual-defect mechanism in rhenium disulfide nanosheets with multi-dimensional ion transport channels for ultrafast sodium storage, Nano Energy 77 (2020) 105189.
[11] M. Sun, X. Wang, J. Wang, H. Yang, L. Wang, T. Liu, Assessment on the self-discharge behavior of lithium−sulfur batteries with $LiNO_3$-possessing electrolytes, ACS Appl. Mater. Interfaces 10 (2018) 35175–35183.
[12] C. Zhao, H. Yang, X. Wang, H. Li, C. Qi, L. Wang, T. Liu, Effect of soluble sulfur species on electrochemical behavior of lithium–sulfur batteries with dual-phase electrolytes, Sustainable Energy Fuels 3 (2019) 1966–1970.
[13] J.S. Lee, W. Kim, J. Jang, A. Manthiram, Sulfur-embedded activated multichannel carbon nanofiber composites for long-life, high-rate lithium–sulfur batteries, Adv. Energy Mater. 7 (2017) 1601943.
[14] D. Xiao, Q. Li, H. Zhang, Y. Ma, C. Lu, C. Chen, Y. Liu, S. Yuan, A sulfur host based on cobalt–graphitic carbon nanocages for high performance lithium–sulfur batteries, J. Mater. Chem. 5 (2017) 24901–24908.
[15] Y. Zhong, X. Xia, S. Deng, J. Zhan, R. Fang, Y. Xia, X. Wang, Q. Zhang, J. Tu, Popcorn inspired porous macrocellular carbon: rapid puffing fabrication from rice and its applications in lithium–sulfur batteries, Adv. Energy Mater. 8 (2018) 1701110.
[16] J. Wang, C. Fu, X. Wang, Y. Yao, M. Sun, L. Wang, T. Liu, Three-dimensional hierarchical porous TiO_2/graphene aerogels as promising anchoring materials for lithium–sulfur batteries, Electrochim. Acta 292 (2018) 568–574.
[17] Z. Li, J. Zhang, X.W. Lou, Hollow carbon nanofibers filled with MnO_2 nanosheets as efficient sulfur hosts for lithium–sulfur batteries, Angew. Chem. Int. Ed. 54 (2015) 12886–12890.
[18] C. Qi, H. Li, J. Wang, C. Zhao, C. Fu, L. Wang, T. Liu, Metal-organic-framework-derived porous carbon embedded with TiO_2 nanoparticles as a cathode for advanced lithium–sulfur batteries, ChemElectroChem 8 (2021) 90–95.
[19] J. Wang, J. Yang, C. Wan, K. De, J. Xie, N. Xu, Sulfur composite cathode materials for rechargeable lithium batteries, Adv. Funct. Mater. 13 (2003) 487–492.
[20] S.S. Zhang, Understanding of sulfurized polyacrylonitrile for superior performance lithium/sulfur battery, Energies 7 (2014) 4588–4600.
[21] X. Wang, Y. Qian, L. Wang, H. Yang, H. Li, Y. Zhao, T. Liu, Sulfurized polyacrylonitrile cathodes with high compatibility in both ether and carbonate electrolytes for ultrastable lithium–sulfur batteries, Adv. Funct. Mater. 29 (2019) 1902929.
[22] S. Wei, L. Ma, K.E. Hendrickson, Z. Tu, L.A. Archer, Metal−sulfur battery cathodes based on PAN−sulfur composites, J. Am. Chem. Soc. 137 (2015) 12143–12152.
[23] J. Fanous, M. Wegner, J. Grimminger, Ä. Andresen, M.R. Buchmeiser, Structure-related electrochemistry of sulfur-poly(acrylonitrile) composite cathode materials for rechargeable lithium batteries, Chem. Mater. 23 (2011) 5024–5028.
[24] J. Fanous, M. Wegner, M.B.M. Spera, M.R. Buchmeiser, High energy density poly (acrylonitrile)-sulfur composite-based lithium-sulfur batteries, J. Electrochem. Soc. 160 (2013) A1169–A1170.
[25] L. Wang, X. He, J. Li, J. Gao, J. Guo, C. Jiang, C. Wan, Analysis of the synthesis process of sulphur–poly(acrylonitrile)-based cathode materials for lithium batteries, J. Mater. Chem. 22 (2012) 22077–22081.
[26] J. Fanous, M. Wegner, J. Grimminger, M. Rolff, M.B.M. Spera, M. Tenzer, M. R. Buchmeiser, Correlation of the electrochemistry of poly(acrylonitrile)–sulfur composite cathodes with their molecular structure, J. Mater. Chem. 22 (2012) 23240–23245.
[27] L. Wang, X. Chen, S. Li, J. Yang, Y. Sun, L. Peng, B. Shan, J. Xie, Effect of eutectic accelerator in selenium-doped sulfurized polyacrylonitrile for high performance room temperature sodium–sulfur batteries, J. Mater. Chem. 7 (2019) 12732–12739.
[28] Z.-Q. Jin, Y.-G. Liu, W.-K. Wang, A.-B. Wang, B.-W. Hu, M. Shen, T. Gao, P.-C. Zhao, Y.-S. Yang, A new insight into the lithium storage mechanism of sulfurized polyacrylonitrile with no soluble intermediates, Energy Storage Mater 14 (2018) 272–278.
[29] X. Huang, J. Liu, Z. Huang, X. Ke, L. Liu, N. Wang, J. Liu, Z. Guo, Y. Yang, Z. Shi, Flexible free-standing sulfurized polyacrylonitrile electrode for stable Li/Na storage, Electrochim. Acta 333 (2020) 135493.
[30] X. Yu, J. Xie, J. Yang, H. Huang, K. Wang, Z. Wen, Lithium storage in conductive sulfur-containing polymers, J. Electroanal. Chem. 573 (2004) 121–128.
[31] A.A. Razzaq, X. Yuan, Y. Chen, J. Hu, Q. Mu, Y. Ma, X. Zhao, L. Miao, J.-H. Ahn, Y. Peng, Z. Deng, Anchoring MOF-derived CoS_2 on sulfurized polyacrylonitrile nanofibers for high areal capacity lithium–sulfur batteries, J. Mater. Chem. 8 (2020) 1298–1306.
[32] M. Frey, R.K. Zenn, S. Warneke, K. Muller, A. Hintennach, R.E. Dinnebier, M. R. Buchmeiser, Easily accessible, textile fiber-based sulfurized poly(acrylonitrile) as Li/S cathode material: correlating electrochemical performance with morphology and structure, ACS Energy Lett 2 (2017) 595–604.
[33] A.A. Razzaq, Y. Yao, R. Shah, P. Qi, L. Miao, M. Chen, X. Zhao, Y. Peng, Z. Deng, High-performance lithium sulfur batteries enabled by a synergy between sulfur and carbon nanotubes, Energy Storage Materials 16 (2019) 194–202.